Viscous Heat Backflow and Temperature Resonances in Extreme Thermal Conductors

Jan Dragašević,[1,*] Bogdan Rajkov,[1] and Michele Simoncelli[1,2,†]
[1]Theory of Condensed Matter Group, Cavendish Laboratory, University of Cambridge, Cambridge, United Kingdom
[2]Department of Applied Physics and Applied Mathematics, Columbia University, New York, New York, USA

(Received 30 May 2023; revised 21 October 2025; accepted 19 December 2025; published 8 May 2026)

We demonstrate that nondiffusive, fluidlike heat transport, such as heat backflowing from cooler to warmer regions, can be induced, controlled, and amplified in extreme thermal conductors such as graphite and hexagonal boron nitride. We employ the viscous heat equations, i.e., the thermal counterpart of the Navier-Stokes equations in the laminar regime, to show with first-principles quantitative accuracy that a finite thermal viscosity yields steady-state heat vortices, and governs the magnitude of transient temperature waves. Finally, we devise strategies that exploit devices' boundaries and resonance to amplify and control heat hydrodynamics, paving the way for novel experiments and applications in next-generation electronic and phononic technologies.

DOI: 10.1103/nbbn-56hr

Introduction—Crystals with ultrahigh thermal conductivity, such as graphite [1–4] and monoisotopic layered hexagonal boron nitride ($h^{11}BN$) [5,6], are critical for copious thermal-management applications in, e.g., electronics and phononics [7,8]. These materials are also of fundamental scientific interest, since they can host heat-transport phenomena that violate Fourier's diffusive law [9–12]. For example, striking hydrodynamiclike phenomena such as temperature waves—where heat transiently backflows from cooler to warmer regions—have recently been observed in graphite up to ∼200 K [13,14]. While technologically promising, these phenomena are weak and difficult to observe; their effective application requires understanding how to induce and control them.

Hitherto, the theoretical analysis of heat hydrodynamics has been done relying on the linearized Peierls-Boltzmann transport equation (LBTE) [15] and on first-principles simulations [7,9,16–20]. These works have provided microscopic insights on hydrodynamic heat transport in three-dimensional [3,5,13,21–24] and two-dimensional [3,19,20,25–30] materials, quantitatively discussing how this emerges from the predominance of momentum-conserving (normal) phonons' collisions over momentum-relaxing (Umklapp) collisions. Under these conditions, the phonons' local equilibrium is described by the drifting distribution, $N^D_{\boldsymbol{q},s}[T(\boldsymbol{r},t),\boldsymbol{u}(\boldsymbol{r},t)]=[\exp(\hbar/[k_B T(\boldsymbol{r},t)][\omega_{\boldsymbol{q}s}-\boldsymbol{q}\cdot\boldsymbol{u}(\boldsymbol{r},t)])-1]^{-1}$ ($\hbar\omega_{\boldsymbol{q}s}$ is the energy of the phonon with crystal momentum $\hbar\boldsymbol{q}$ and mode s), which is parametrized not only by a local temperature $T(\boldsymbol{r},t)$ (emerging from the conservation of energy in all phonon collisions), but also by a drift velocity $\boldsymbol{u}(\boldsymbol{r},t)$ that emerges from the conservation of crystal momentum in the dominant normal collisions. While the LBTE has provided insights on heat hydrodynamic phenomena such as second sound (temperature oscillations) [11,13,25] and Poiseuille-like heat flow [10,19,23,31–33], its complexity and high computational cost hinder its use in exploring new hallmarks of heat hydrodynamics. Recent research has focused on developing mesoscopic models that capture the physics governing heat hydrodynamics at reduced complexity and cost; in practice, these are obtained by marginalizing the microscopic (phonon) degrees of freedom in the LBTE, thus describing only the evolution of local-equilibrium fields (T and $\boldsymbol{u}$) [34–38].

Viscous heat equations—Reference [37] has shown how the symmetries of the microscopic LBTE imply that two transport coefficients are needed to describe thermal transport from the diffusive to the laminar hydrodynamic regime. The first one is the well-known thermal conductivity tensor κ^{ij} (i, j are Cartesian indices), which originates from the odd-parity part of the LBTE's solution, and quantifies the response of the crystal to a temperature perturbation. The second one, the thermal viscosity tensor η^{ijkl}, emerges from the even-parity part; this is usually neglected but becomes relevant in the hydrodynamic regime, quantifying the response to a drift-velocity perturbation. Conductivity and viscosity parametrize two coupled viscous heat equations (VHE) describing the evolution of

*Present address: Theoretical Quantum Optics group, Center for Hybrid Quantum Networks, Niels Bohr Institute, University of Copenhagen (DK), Copenhagen, Denmark.
†Contact author: michele.simoncelli@columbia.edu

Published by the American Physical Society under the terms of the Creative Commons Attribution 4.0 International license. Further distribution of this work must maintain attribution to the author(s) and the published article's title, journal citation, and DOI.

$T(\boldsymbol{r},t)$ and $\boldsymbol{u}(\boldsymbol{r},t)$ in the linear regime close to equilibrium (repeated indices are summed),

$$C\frac{\partial T(\boldsymbol{r},t)}{\partial t}+\alpha^{ij}\frac{\partial u^j(\boldsymbol{r},t)}{\partial r^i}-\kappa_D^{ij}\frac{\partial^2 T(\boldsymbol{r},t)}{\partial r^i\partial r^j}=\dot{q}(\boldsymbol{r},t), \quad (1)$$

$$A^{ij}\frac{\partial u^j(\boldsymbol{r},t)}{\partial t}+\beta^{ij}\frac{\partial T(\boldsymbol{r},t)}{\partial r^j}-\eta^{ijkl}\frac{\partial^2 u^k(\boldsymbol{r},t)}{\partial r^j\partial r^l}=-\gamma^{ij}u^j(\boldsymbol{r},t), \quad (2)$$

where C is the specific heat; $A^{ij}=A^i\delta^{ij}$ is a matrix having zero off-diagonal elements and the specific momentum in direction i, A^i, on the diagonal; α^{ij} and β^{ij} are coupling tensors that originate from the relation between crystal momentum and energy for phonons; γ^{ij} describes the dissipation of crystal momentum due to Umklapp processes (this term is weak in the hydrodynamic regime and becomes strong in the diffusive regime, implying that in the latter the VHE reduce to Fourier's law); $\kappa_D^{ij}=\kappa^{ij}-\alpha^{ik}[\gamma^{-1}]^{kl}\beta^{lj}$ is the conductivity contribution from diffusion-damped relaxons, see Supplemental Material for details [39]; $\dot{q}(\boldsymbol{r},t)$ describes the energy exchange with a localized external heater. All these parameters can be determined from the LBTE, accounting for the actual material's phonon band structure and full collision matrix with first-principles accuracy; in the regime where phonon mean free paths are comparable to the device size, they are subject to a Bosanquet-type rescaling, analogously to rarefied fluids [40,130] (see Supplemental Material [39]). Finally, we recall that within the VHE the total heat flux originates from temperature gradient and drift velocity: $\boldsymbol{Q}^{\mathrm{TOT}}=\boldsymbol{Q}^{\delta}+\boldsymbol{Q}^{D}$ where $Q^{\delta,i}=-\kappa_D^{ij}\nabla^j T$ and $Q^{D,i}=\alpha^{ij}u^j$.

The VHE encompass, as special limiting cases, Fourier's equation for heat diffusion, the dual-phase-lag equation (DPLE) [41,42] for second sound [131], and the Guyer-Krumhansl Equation (GKE) [43] for phonon hydrodynamics in idealized materials with linear-isotropic phonon dispersion. Fourier's limit emerges when Umklapp dissipation $\gamma^{ij}u^j(\boldsymbol{r},t)$ dominates over viscous effects $\eta^{ijkl}\partial_{r^j}\partial_{r^l}u^k(\boldsymbol{r},t)$ [37], while the DPLE describes temperature waves in the transient inviscid limit ($\eta^{ijkl}=0$), see Supplemental Material II for a proof [39]. Both limits are obtained when viscous effects are negligible, the former in the steady-state and the latter in the transient domain. On the other hand, the GKE include a viscous term, but they cannot be applied to realistic materials with nonlinear phonon dispersions (see Supplemental Material III [39]). Thus, understanding how thermal viscosity influences hydrodynamic transport signatures in steady-state and transient regimes is an open fundamental question. Here we address these questions, investigating from first principles how to induce, amplify, and control viscous heat hydrodynamics in graphite at various isotopic purities, as well as in $h^{11}BN$ [132].

Steady-state viscous heat backflow—In Fig. 1 we investigate how viscosity affects steady-state thermal transport by comparing the numerical solution of Fourier's (inviscid) equation (panel a) with that of the viscous VHE (panel b). We consider a graphitic device with a tunnel-chamber geometry [133], which promotes vortical hydrodynamic behavior (more on this later). We highlight that the VHE temperature profile in the chamber is reversed compared to the profile in the tunnel, a behavior completely opposite to that predicted by Fourier's law. Panel c shows that this temperature inversion—which in principle can be detected in thermal-imaging experiments [44,134–139]—occurs in the presence of viscous vortical flow, when heat backflows against the temperature gradient. In Supplemental Material VI [39] we show that heat vortices are not limited to graphite, predicting them also in $h^{11}BN$ around 60 K.

To see how the emergence of heat backflow in Fig. 1 requires the presence of a finite thermal viscosity, we start

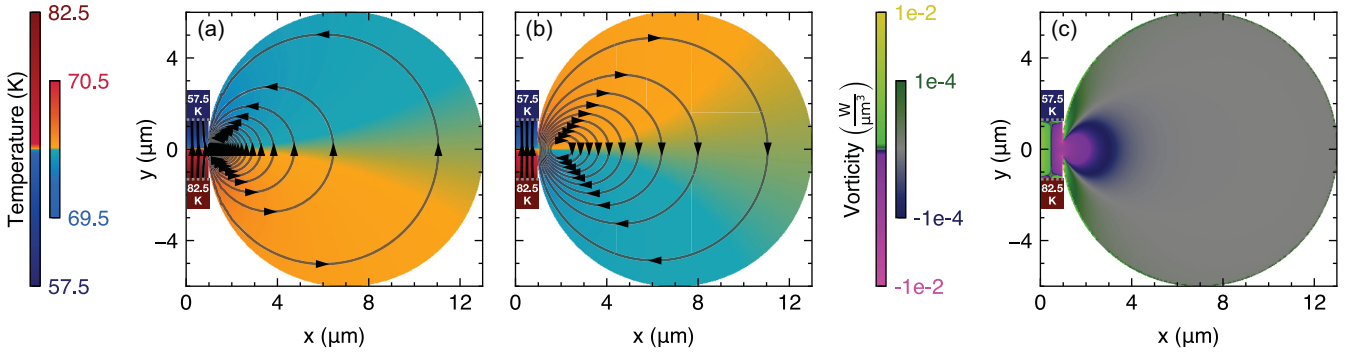


FIG. 1. Viscous heat backflow and temperature inversion. In-plane heat flow streamlines and temperature in a graphitic tunnel-chamber device. (a),(b) Show the solution of Fourier's equation and VHE, respectively, when a temperature gradient is applied to the tunnel ($T=70\pm12.5$ K at $y=\mp1.25$ μm); the other boundaries are adiabatic, and in the VHE they have a finite-slip length of 0.4 μm [140], corresponding to diffusive phonon-boundary scattering (see End Matter). In Fourier's case (a) the temperature gradient in the chamber and in the tunnel have the same direction, while in the VHE (b) these temperature gradients are inverted due to the presence of heat backflow. (c) Vorticity of the VHE heat flux, $\nabla\times\boldsymbol{Q}^{\mathrm{TOT}}$; in Fourier's case, vorticity is zero.

from Eqs. (1) and (2) in the steady state and focus on geometries for which transport is isotropic (e.g., graphite and $h^{11}BN$ in the in-plane directions). Then, considering the inviscid limit, Eq. (2) reduces to $\beta^{ij}\nabla^j T(\boldsymbol{r},t) = -\gamma^{ij}u^j(\boldsymbol{r},t)$, and using this in Eq. (1) readily shows that this inviscid limit is governed by a Fourier-like irrotational equation, where the total heat flux is exclusively determined by the temperature gradient and thus, vortices and backflow cannot emerge [141]. In contrast, when viscosity is nonzero, in Eq. (2) $\boldsymbol{u}$ is no longer proportional to ∇T, and thus the total heat flux $\boldsymbol{Q}^{\mathrm{TOT}}$ cannot be simplified to an irrotational expression. This demonstrates that viscosity is necessary to have vorticity and steady-state heat backflow. However, a nonzero viscosity is not sufficient to observe heat backflow; in fact, one also needs a device's geometry and boundary conditions (BCs) that permit nonzero second derivative of $\boldsymbol{u}$, i.e., of a vortical total heat flow. In this regard, we discuss in Supplemental Material VII [39] how the tunnel-chamber geometry can drive inhomogeneities in $\boldsymbol{u}$ that are sufficient to produce viscous backflow and temperature inversion, and analyze in the End Matter how the latter is influenced by the BCs. In Supplemental Material VIII [39] we discuss how backflow depends on the device's size, average temperature, and isotopes.

Transient viscous heat backflow—Experiments in graphite have observed heat backflowing against the temperature gradient only in the time-dependent domain, in the form of second sound [11,13] or lattice cooling [12]. Pioneering simulations have been performed relying on the microscopic LBTE [11–13,142] without resolving effects induced by the thermal viscosity, or relying on the inviscid DPLE [41,42,45–50]. It is therefore natural to wonder how the viscous heat backflow emerging from the VHE behaves in the time domain, and, more precisely, if there is a relationship between temperature waves and transient viscous heat backflow. Therefore, we perform a time-dependent simulation, considering a rectangular device initially at equilibrium ($T = 80$ K [143] and $\boldsymbol{u} = \boldsymbol{0}$); we perturb it with a heater localized at ($x_c = 5$ μm, 0) for $0 < t < t_{\mathrm{heat}}$ (accounted for by $\dot{q}(\boldsymbol{r},t)$ in Eq. (1), see Ref. [144]); at $t = t_{\mathrm{heat}}$ we switch off the heater and monitor the relaxation (Fig. 2). The device is always thermalized at the boundaries ($T = 80$ K and $\boldsymbol{u} = \boldsymbol{0}$), see Ref. [44] for an experimental example of this BC, and Supplemental Material X [39] for details on how BCs (average temperature and thermalization length scale), size, and isotopic disorder affect the relaxation. The VHE evolution of temperature (Fig. 2) shows an oscillatory behavior, with the local appearance of values lower than the initial temperature. In contrast, we show in Supplemental Material XI [39] that, in Fourier's law, a positive temperature perturbation relaxes remaining non-negative with respect to the initial equilibrium value (a consequence of the smoothing property of the diffusion equation [51]).

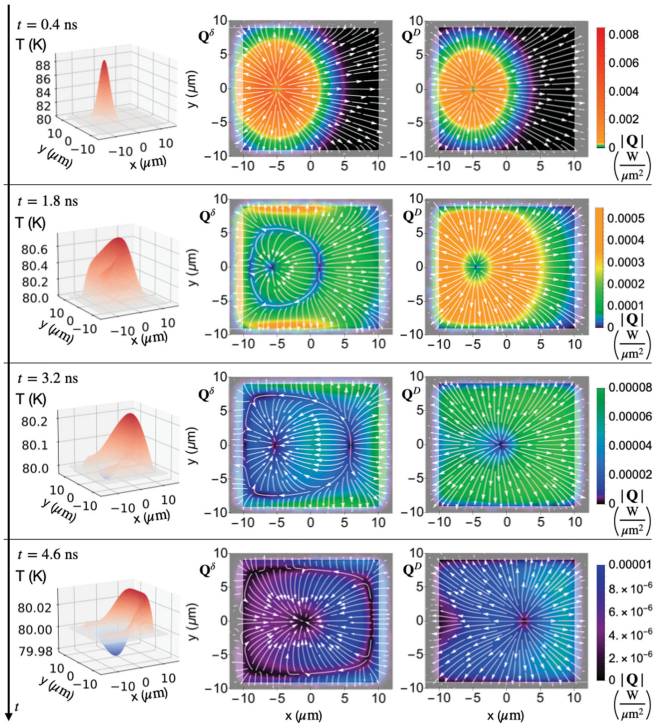


FIG. 2. Transient viscous heat backflow. Columns show temperature (left), temperature-gradient heat flux ($\boldsymbol{Q}^{\delta}$, center), and drifting heat flux ($\boldsymbol{Q}^{D}$, right) at different times (relaxation starts at $t = 0.4$ ns, see text), and are obtained solving the VHE in a graphitic device thermalized at 80 K in the shaded boundary regions. In the 2D plots, color is the heat-flux modulus, and white streamlines show its direction.

To understand what drives the emergence of heat backflow, we analyze the evolution of the heat-flux components $\boldsymbol{Q}^{\delta}$ and $\boldsymbol{Q}^{D}$. Their streamlines in the second and third column of Fig. 2 show that $\boldsymbol{Q}^{\delta}$ and $\boldsymbol{Q}^{D}$ can assume opposite directions during the relaxation, with the drifting flux $\boldsymbol{Q}^{D} \propto \boldsymbol{u}$ backflowing against the temperature-gradient flux $\boldsymbol{Q}^{\delta} \propto -\nabla T$. This is a consequence of the delayed coupling between $\boldsymbol{Q}^{\delta}$ and $\boldsymbol{Q}^{D}$ in the VHE (1), (2), which, in the inviscid limit $\eta^{ijkl} = 0$, reduces to the lagged relationship between heat flux and temperature gradient described by the DPLE [42], details in Supplemental Material II [39]. This also shows that while steady-state heat backflow can emerge exclusively as a consequence of a finite viscosity, transient backflow does not necessarily require viscosity to appear (Supplemental Material XI [39]). Nevertheless, we will show that it is necessary to consider viscous effects to rationalize experiments.

Resonant amplification of temperature waves—The temperature waves observed in Fig. 2 have a small amplitude, hence they are difficult to detect. Nevertheless, they are expected to exhibit resonant amplification when driven by a perturbation periodic in time, and this could be exploited to facilitate their observation and control. Therefore, we investigate the behavior of the device in

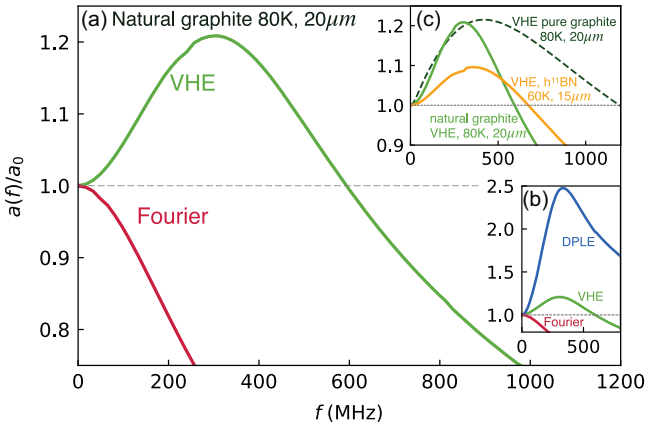


FIG. 3. Resonant amplification of temperature waves in graphite at natural isotopic disorder (98.9% ^{12}C, 1.1% ^{13}C) and around $T = 80$ K (a); the prediction from the viscous VHE is green, red is Fourier's law, and the DPLE is reported in inset (b). Inset (c), the VHE predict that isotopically purified graphite (99.9% ^{12}C, 0.1% ^{13}C, dashed dark green) features a stronger resonant amplification compared to natural graphite (solid green); in addition, analogous signatures are predicted to appear in h^{11}BN, around $T = 60$ K in 15 μm-long devices.

Fig. 2 when driven by a periodic perturbation. Considering the analogies between temperature and mechanical waves, we applied to the device in Fig. 2 a periodic two-spot perturbation mathematically similar to the (1, 2) mode of a loaded rectangular membrane [145]. This perturbation is always non-negative, consistent with the laser heating employed in experiments [11–13]. Then, we monitored how the amplitude of the temperature oscillation, a, varies as a function of frequency, f. Figure 3 shows that the solution of the periodically driven VHE in natural graphite displays resonant behavior, i.e., plotting the oscillation amplitude as a function of frequency, $a(f)$, we see a peak reminiscent of that observed in the frequency response of a driven underdamped oscillator. We highlight how the resonant behavior obtained from the viscous VHE is weaker than that obtained from the inviscid DPLE [45,49,52], while Fourier's law does not show a resonant response (analogously to an overdamped oscillator). Finally, the insets show that reducing isotope disorder in graphite yields a stronger resonant response, and that analogous signatures are predicted in h^{11}BN.

Next, we investigate how the resonant amplification varies as a function of device size, average temperature, and type of material. We performed simulations analogous to Fig. 3 varying device's size [146] and equilibrium temperature, computing for every simulation the maximum resonant amplification as $\max_f[a(f)]/a_0$ (where $a_0 = \lim_{f\to 0} a(f)$, see Fig. 3). In Figs. 4(a) and 4(b) we compare the inviscid DPLE (a) with the VHE (b) in natural graphite. We see that the temperatures and length scales at which the VHE predict the emergence of hydrodynamic resonance in natural samples are in broad agreement with experiments [11]; in contrast, the DPLE fails to capture the reduction of hydrodynamic behavior below 100 K. In isotopically purified graphite [Fig. 4(c)], we see that the VHE resonant response is stronger than in natural graphite, and it also persists up to larger length scales and higher temperatures, in broad agreement with experiments [13,147]. Finally, Fig. 4(d) predicts that hydrodynamic temperature resonances also occur in h^{11}BN, with a magnitude slightly weaker than in natural graphite.

Comparison between VHE and microscopic LBTE—We recall that the VHE are obtained by coarse graining the LBTE for the phonon distribution and evaluating transport coefficients from homogeneous linear response, i.e., neglecting spatial and temporal gradients of the out-of-equilibrium phonon distribution [37]. The VHE are thus most accurate when these gradients are small. To verify our approach at the length and time scales considered here, we compared our steady-state and transient VHE solutions with the corresponding ones obtained by solving the LBTE with the full collision operator [53] (Fig. 5 and Supplemental Material XII [39], respectively). In both cases, the LBTE confirms the signatures predicted by the VHE.

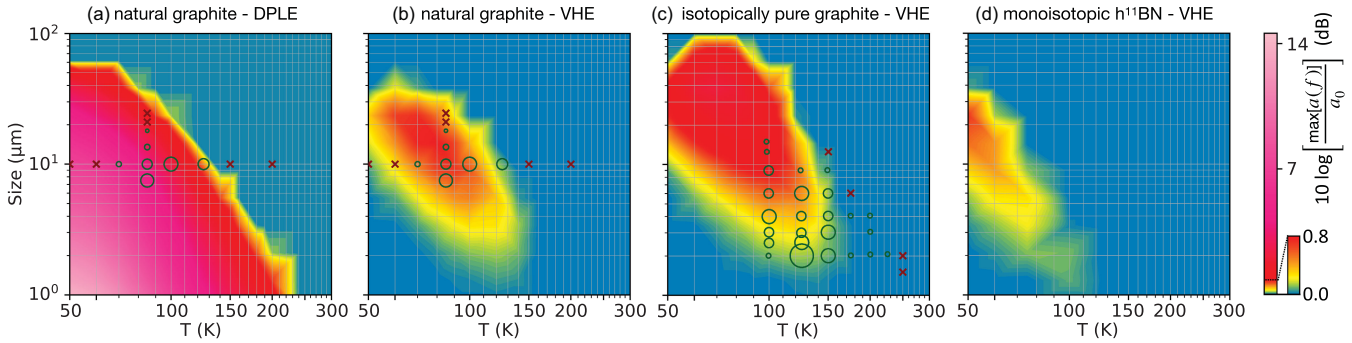


FIG. 4. Maximum resonant amplification as a function of size, average temperature, and isotopic disorder. (a),(b) show the DPLE (VHE) in natural graphite; empty green circles have an area proportional to the hydrodynamic strength [148] measured in experiments [11], red crosses correspond to diffusive behavior (no hydrodynamics). (c) VHE simulations for isotopically purified graphite, with experiments from Ref. [13]. (d) VHE resonant behavior in h^{11}BN.

Conclusion—We have shed light on the fundamental physics determining the emergence of viscous heat hydrodynamics, discussing with quantitative first-principles accuracy how in extreme thermal conductors such as graphite and layered $h^{11}BN$ it is possible to induce temperature inversion from steady-state heat vortices, and viscous temperature waves. We have demonstrated that these phenomena can be amplified by engineering the device's geometry, boundary conditions, or exploiting resonance, paving the way for applications in next-generation technologies. We have shown that the viscous temperature waves emerging from the VHE differ fundamentally from the inviscid heat waves discussed in past works [41,42,45,49,52]. We have quantitatively shown that viscous effects determine the hydrodynamic relaxation timescales [12] and length scales [11,13] measured in pioneering experiments. From a technological perspective, this Letter identifies the conditions under which heat conduction violates the smoothing property of Fourier's equation, opening new avenues to engineer thermal signals for heat-based neuromorphic computing [149,150].

Acknowledgments—We thank M. Beneitez, G. Conduit, and O. Scarlatella for commenting the manuscript, as well as S. Huberman, A. Sokolov, and E. Di Lucente for the useful discussions. M. S. acknowledges support from: Gonville and Caius College; the SNSF Project No. P500PT_203178; the Sulis Tier 2 HPC platform (funded by EPSRC Grant No. EP/T022108/1 and the HPC Midlands+ consortium); the Kelvin2 HPC platform at the NI-HPC Centre (funded by EPSRC, managed by Queen's University Belfast and Ulster University). B. R. acknowledges support from Trinity College, Cambridge. J. D. thanks H. Jasak for the hospitality in Cambridge.

Data availability—The data that support the findings of this article are openly available [151], embargo periods may apply.

[1] A. J. Schmidt, X. Chen, and G. Chen, Rev. Sci. Instrum. **79**, 114902 (2008).
[2] A. A. Balandin, Nat. Mater. **10**, 569 (2011).
[3] G. Fugallo, A. Cepellotti, L. Paulatto, M. Lazzeri, N. Marzari, and F. Mauri, Nano Lett. **14**, 6109 (2014).
[4] Y. Machida, N. Matsumoto, T. Isono, and K. Behnia, Science **367**, 309 (2020).
[5] P. Jiang, X. Qian, R. Yang, and L. Lindsay, Phys. Rev. Mater. **2**, 064005 (2018).
[6] C. Yuan, J. Li, L. Lindsay, D. Cherns, J. W. Pomeroy, S. Liu, J. H. Edgar, and M. Kuball, Commun. Phys. **2** (2019).
[7] X. Qian, J. Zhou, and G. Chen, Nat. Mater. **20**, 1188 (2021).
[8] S. Moon, J. Kim, J. Park, S. Im, J. Kim, I. Hwang, and J. K. Kim, Adv. Mater. **35**, 2204161 (2023).
[9] G. Chen, Nat. Rev. Phys. **3**, 555 (2021).
[10] X. Huang, Y. Guo, Y. Wu, S. Masubuchi, K. Watanabe, T. Taniguchi, Z. Zhang, S. Volz, T. Machida, and M. Nomura, Nat. Commun. **14**, 2044 (2023).
[11] S. Huberman, R. A. Duncan, K. Chen, B. Song, V. Chiloyan, Z. Ding, A. A. Maznev, G. Chen, and K. A. Nelson, Science **364**, 375 (2019).
[12] J. Jeong, X. Li, S. Lee, L. Shi, and Y. Wang, Phys. Rev. Lett. **127**, 085901 (2021).
[13] Z. Ding, K. Chen, B. Song, J. Shin, A. A. Maznev, K. A. Nelson, and G. Chen, Nat. Commun. **13**, 285 (2022).
[14] Specifically, Ref. [13] observed temperature oscillations at temperatures as high as 200 K in isotopically purified graphite, while the pioneering works [11,12] observed temperature oscillations around 80–125 K in graphite at natural isotopic abundance.
[15] R. E. Peierls, *Quantum Theory of Solids* (Oxford University Press, New York, 1955).
[16] L. Lindsay, A. Katre, A. Cepellotti, and N. Mingo, J. Appl. Phys. **126**, 050902 (2019).
[17] L. Chaput, Phys. Rev. Lett. **110**, 265506 (2013).
[18] G. Fugallo, M. Lazzeri, L. Paulatto, and F. Mauri, Phys. Rev. B **88**, 045430 (2013).
[19] S. Lee, D. Broido, K. Esfarjani, and G. Chen, Nat. Commun. **6**, 6290 (2015).
[20] A. Cepellotti and N. Marzari, Phys. Rev. X **6**, 041013 (2016).
[21] Z. Ding, J. Zhou, B. Song, V. Chiloyan, M. Li, T.-H. Liu, and G. Chen, Nano Lett. **18**, 638 (2018).
[22] Y. Guo, Z. Zhang, M. Bescond, S. Xiong, M. Wang, M. Nomura, and S. Volz, Phys. Rev. B **104**, 075450 (2021).
[23] X. Li, H. Lee, E. Ou, S. Lee, and L. Shi, J. Appl. Phys. **131**, 075104 (2022).
[24] X. Huang, Y. Guo, S. Volz, and M. Nomura, Appl. Phys. Express **15**, 105001 (2022).
[25] A. Cepellotti, G. Fugallo, L. Paulatto, M. Lazzeri, F. Mauri, and N. Marzari, Nat. Commun. **6**, 6400 (2015).
[26] A. K. Majee and Z. Aksamija, Phys. Rev. B **98**, 024303 (2018).
[27] M. Raya-Moreno, J. Carrete, and X. Cartoixà, Phys. Rev. B **106**, 014308 (2022).
[28] Y. Guo, Z. Zhang, M. Nomura, S. Volz, and M. Wang, Int. J. Heat Mass Transfer **169**, 120981 (2021).
[29] C. Zhang, S. Huberman, and L. Wu, J. Appl. Phys. **132**, 085103 (2022).
[30] Z. Han and X. Ruan, Phys. Rev. B **108**, L121412 (2023).
[31] A. Cepellotti and N. Marzari, Nano Lett. **17**, 4675 (2017).
[32] Y. Machida, A. Subedi, K. Akiba, A. Miyake, M. Tokunaga, Y. Akahama, K. Izawa, and K. Behnia, Sci. Adv. **4**, eaat3374 (2018).
[33] L. Sendra, A. Beardo, J. Bafaluy, P. Torres, F. X. Alvarez, and J. Camacho, Phys. Rev. B **106**, 155301 (2022).
[34] X. Li and S. Lee, Phys. Rev. B **97**, 094309 (2018).
[35] Y. Guo, D. Jou, and M. Wang, Phys. Rev. B **98**, 104304 (2018).
[36] M.-Y. Shang, C. Zhang, Z. Guo, and J.-T. Lü, Sci. Rep. **10**, 8272 (2020).
[37] M. Simoncelli, N. Marzari, and A. Cepellotti, Phys. Rev. X **10**, 011019 (2020).
[38] L. Sendra, A. Beardo, P. Torres, J. Bafaluy, F. X. Alvarez, and J. Camacho, Phys. Rev. B **103**, L140301 (2021).

[39] See Supplemental Material at http://link.aps.org/supplemental/10.1103/nbbn-56hr for derivations of selected expressions from the main text, discussion of the equations and parameters used in the simulations, methodological and computational details, and additional results supporting the main conclusions of the article. It also includes Refs. [5,6,11–13,17,18,20,33,37,38,40–54,70,73–129,140].
[40] V. K. Michalis, A. N. Kalarakis, E. D. Skouras, and V. N. Burganos, Microfluid. Nanofluid. **9**, 847 (2010).
[41] D. D. Joseph and L. Preziosi, Rev. Mod. Phys. **61**, 41 (1989).
[42] D. Y. Tzou, J. Heat Transfer **117**, 8 (1995).
[43] R. A. Guyer and J. A. Krumhansl, Phys. Rev. **148**, 766 (1966).
[44] O. Braun, R. Furrer, P. Butti, K. Thodkar, I. Shorubalko, I. Zardo, M. Calame, and M. L. Perrin, npj 2D Mater. Appl. **6**, 1 (2022).
[45] M. Xu and L. Wang, Int. J. Heat Mass Transfer **45**, 1055 (2002).
[46] J. Ordóñez-Miranda and J. J. Alvarado-Gil, Mech. Res. Commun. **37**, 276 (2010).
[47] Z. Kang, P. Zhu, D. Gui, and L. Wang, Int. J. Heat Mass Transfer **115**, 250 (2017).
[48] M. Gandolfi, G. Benetti, C. Glorieux, C. Giannetti, and F. Banfi, Int. J. Heat Mass Transfer **143**, 118553 (2019).
[49] M. Xu, Proc. Math. Phys. Eng. **477**, 20200913 (2021).
[50] G. Mazza, M. Gandolfi, M. Capone, F. Banfi, and C. Giannetti, Nat. Commun. **12**, 6904 (2021).
[51] D. Skinner, *Mathematical Methods* (University of Cambridge, Cambridge, 2015).
[52] A. Barletta and E. Zanchini, Int. J. Heat Mass Transfer **39**, 1307 (1996).
[53] M. Raya-Moreno, X. Cartoixà, and J. Carrete, Comput. Phys. Commun. **281**, 108504 (2022).
[54] M. Raya-Moreno, Ph.D. thesis, Universitat Autònoma de Barcelona, 2022.
[55] F. F. M. Sabatti, S. M. Goodnick, and M. Saraniti, J. Heat Transfer **139**, 032002 (2016).
[56] Implemented in BTE-BARNA following Sec. 4.2.2.1 of [54].
[57] J. Laurent, A. Drezet, H. Sellier, J. Chevrier, and S. Huant, Phys. Rev. Lett. **107**, 164501 (2011).
[58] O. D. Gurcan, P. H. Diamond, X. Garbet, V. Berionni, G. Dif-Pradalier, P. Hennequin, P. Morel, Y. Kosuga, and L. Vermare, Phys. Plasmas **20**, 022307 (2013).
[59] P. B. Allen, Phys. Rev. B **97**, 134307 (2018).
[60] M.-Y. Shang, W.-H. Mao, N. Yang, B. Li, and J.-T. Lü, Phys. Rev. B **105**, 165423 (2022).
[61] U. Yadav, C. N. S. Goutham, K. Meshram, A. Pathak, D. Bansal, and A. Agrawal, Phys. Rev. Appl. **24**, 034024 (2025).
[62] M. L. Palm, C. Ding, W. S. Huxter, T. Taniguchi, K. Watanabe, and C. L. Degen, Science **384**, 465 (2024).
[63] J. Coulter, R. Sundararaman, and P. Narang, Phys. Rev. B **98**, 115130 (2018).
[64] U. Vool, A. Hamo, G. Varnavides, Y. Wang, T. X. Zhou, N. Kumar, Y. Dovzhenko, Z. Qiu, C. A. C. Garcia, A. T. Pierce, J. Gooth, P. Anikeeva, C. Felser, P. Narang, and A. Yacoby, Nat. Phys. **17**, 1216 (2021).
[65] H.-Y. Yang, X. Yao, V. Plisson, S. Mozaffari, J. P. Scheifers, A. F. Savvidou, E. S. Choi, G. T. McCandless, M. F. Padlewski, C. Putzke, P. J. W. Moll, J. Y. Chan, L. Balicas, K. S. Burch, and F. Tafti, Nat. Commun. **12**, 5292 (2021).
[66] A. Jaoui, A. Gourgout, G. Seyfarth, A. Subedi, T. Lorenz, B. Fauqué, and K. Behnia, Phys. Rev. X **12**, 031023 (2022).
[67] X. Huang and A. Lucas, Phys. Rev. B **103**, 155128 (2021).
[68] N. H. Protik, C. Li, M. Pruneda, D. Broido, and P. Ordejón, npj Comput. Mater. **8**, 28 (2022).
[69] A. Levchenko and J. Schmalian, Ann. Phys. (Amsterdam) **419**, 168218 (2020).
[70] J. Coulter, B. Rajkov, and M. Simoncelli, arXiv:2503.07560.
[71] X.-Y. Wei, O. A. Santos, C. H. S. Lusero, G. E. W. Bauer, J. Ben Youssef, and B. J. van Wees, Nat. Mater. **21**, 1352 (2022).
[72] H. D. Rosales, F. A. G. Albarracín, P. Pujol, and L. D. C. Jaubert, Phys. Rev. Lett. **130**, 106703 (2023).
[73] H. Spohn, J. Stat. Phys. **124**, 1041 (2006).
[74] One can also directly see that $\langle\theta^0_\nu|v^i_\nu|\theta^0_\nu\rangle \propto \sum_s \int_{\mathfrak{B}} \omega^2_{\mathbf{q}s} v^i_{\mathbf{q}s} d^3q = 0$, because it is obtained by integrating an odd-parity integrand over the symmetric Brillouin zone $\mathfrak{B}$.
[75] The relaxon [20] and variational [18] methods always provide results that are numerically compatible within 0.1%. For example, in natural graphite at 80 K the bulk thermal conductivity obtained from the variational method [18] at 80 K is 5735.08 W/mK while with the relaxon formalism it is 5735.03 W/mK; in isotopically purified graphite (99.9% ^{12}C, 0.1% ^{13}C) the bulk thermal conductivity at 80 K obtained from the variational method is 27484.96 W/mK while with the relaxon formalism it is 27485.09 W/mK; for h^{11}BN the variational method at 60 K yields 3944.20 W/mK, while the result of the relaxon method is 3944.23 W/mK.
[76] P. B. Allen and V. Perebeinos, Phys. Rev. B **98**, 085427 (2018).
[77] J. M. Ziman, *Electrons and Phonons: The Theory of Transport Phenomena in Solids* (Oxford University Press, New York, 1960).
[78] R. Winkler, *Spin-Orbit Coupling Effects in Two-Dimensional Electron and Hole Systems* (Springer, Berlin/Heidelberg, 2003).
[79] S. Bravyi, D. P. DiVincenzo, and D. Loss, Ann. Phys. (Amsterdam) **326**, 2793 (2011).
[80] R. A. Horn and C. R. Johnson, *Topics in Matrix Analysis* (Cambridge University Press, Cambridge, England, 1991).
[81] Specifically, Eq. (0.7.3.1) of Ref. [80] shows that for a partitioned nonsingular matrix A,

$$A = \begin{bmatrix} A_{11} & A_{12} \\ A_{21} & A_{22} \end{bmatrix} \tag{3}$$

its inverse can be written in partitioned form as,

$$A^{-1} = \begin{bmatrix} (A_{11} - A_{12}A_{22}^{-1}A_{21})^{-1} & A_{11}^{-1}A_{12}(A_{21}A_{11}^{-1}A_{12} - A_{22})^{-1} \\ A_{22}^{-1}A_{21}(A_{12}A_{22}^{-1}A_{21} - A_{11})^{-1} & (A_{22} - A_{21}A_{11}^{-1}A_{12})^{-1} \end{bmatrix}. \tag{4}$$

[82] R. N. Gurzhi, Sov. Phys. Usp. **11**, 255 (1968).
[83] D. A. Bandurin, I. Torre, R. K. Kumar, M. Ben Shalom, A. Tomadin, A. Principi, G. H. Auton, E. Khestanova, K. S. Novoselov, I. V. Grigorieva, L. A. Ponomarenko, A. K. Geim, and M. Polini, Science **351**, 1055 (2016).
[84] R. Kovács, A. Fehér, and S. Sobolev, Int. J. Heat Mass Transfer **194**, 123021 (2022).
[85] R. Sambasivam, S. Chakraborty, and F. Durst, Microfluid. Nanofluid. **16**, 757 (2014).
[86] The volume viscosity is also called the bulk viscosity, here we use the term "bulk viscosity" for the value of the viscosity tensor in the bulk of the crystal, without accounting for finite size effects.
[87] L. Landau and E. Lifshitz, *Fluid Mechanics* (Pergamon Press, New York, 1987).
[88] S. De Groot and P. Mazur, *Non-Equilibrium Thermodynamics*, Dover Books on Physics (Dover Publications, New York, 2013).
[89] C. Q. Cook and A. Lucas, Phys. Rev. B **99**, 235148 (2019).
[90] Strictly speaking, in proximity of a perfectly thermalized boundary (temperature fixed at a certain value and $\boldsymbol{u} = \boldsymbol{0}$), the temperature gradient emerging from the VHE is weakly space dependent, due to the coupling between the temperature gradient and the drift velocity in Eq. (2). In practice, in a rectangular geometry of graphite with gradient applied around 70 K, the temperature gradient and drift velocity reach a practically space-independent value within about 1 μm from the boundaries. Analytical details on the mechanisms determining this length scale can be found in Appendix G of Ref. [37], and numerical simulations in Fig. 4 of the same reference.
[91] For a well-behaved vector field, the circulation computed on a closed streamline $\vec{\mathcal{S}}$ is nonzero: $\mathcal{C} = \oint_{\mathcal{S}} \boldsymbol{Q}^D \cdot d\vec{\mathcal{S}} \neq 0$; therefore, one sees from Stokes's theorem that this implies nonzero vorticity: $\mathcal{C} = \int_{\mathcal{A}} (\nabla \times \boldsymbol{Q}^D) \cdot \boldsymbol{m} d\mathcal{A} \neq 0$, where $\boldsymbol{m}$ is the unit vector outward normal to the surface $\mathcal{A}$ enclosed by $\vec{\mathcal{S}}$.
[92] Specifically, in the region where temperature inversion is most pronounced in Fig. 1, one has $\beta\{[\partial T(\boldsymbol{r}, t)]/(\partial r^y)\} \sim \eta^{yyyy}\{[\partial^2 u^y(\boldsymbol{r}, t)]/(\partial r_y^2)\}$, a condition that permits temperature gradient and drift velocity to be aligned, thus temperature-gradient heat flux $\boldsymbol{Q}^\delta = -\kappa_D \nabla T$ and drifting heat flux $\boldsymbol{Q}^D = \alpha \boldsymbol{u}$ to have opposite directions.
[93] J. D. Hunter, Comput. Sci. Eng. **9**, 90 (2007).
[94] Matplotlib Developers (2023), https://github.com/matplotlib/matplotlib/issues/27261 (Accessed: 2025).
[95] J.-P. M. Péraud and N. G. Hadjiconstantinou, Phys. Rev. B **84**, 205331 (2011).
[96] The VHE solution in Fig. 1 was computed in less than two minutes on a laptop, while the corresponding LBTE solution in Fig. 5 took about 72 hours on one node (128 cores) of the Kelvin2 supercomputer from the Northern Ireland High Performance Computing center.
[97] L. Paulatto, F. Mauri, and M. Lazzeri, Phys. Rev. B **87**, 214303 (2013).
[98] L. Paulatto, I. Errea, M. Calandra, and F. Mauri, Phys. Rev. B **91**, 054304 (2015).
[99] A. Togo, J. Phys. Soc. Jpn. **92**, 012001 (2023).
[100] https://phonopy.github.io/phonopy/qe.html.
[101] anharmonic, (2013), https://github.com/anharmonic/d3q/tree/main/thermal2 (Accessed: 2023).
[102] W. Li, J. Carrete, N. A. Katcho, and N. Mingo, Comput. Phys. Commun. **185**, 1747 (2014).
[103] S.-i. Tamura, Phys. Rev. B **27**, 858 (1983).
[104] C. Greenshields, https://openfoam.org (2024), https://doc.cfd.direct/openfoam/user-guide-v12/boundaries (Accessed: 2024).
[105] L. W. Tu, *An Introduction to Manifolds* (Springer Science+Business Media, LLC, New York, NY, 2008), pp. 127–130, 10.1007/978-1-4419-7400-6.
[106] F. Phillips, https://resources.wolframcloud.com/FunctionRepository/resources/SmootherStep/ (2019).
[107] P. Carruthers, Rev. Mod. Phys. **33**, 92 (1961).
[108] A. Cepellotti and N. Marzari, Phys. Rev. Mater. **1**, 045406 (2017).
[109] M. Simoncelli, N. Marzari, and F. Mauri , Nat. Phys. **15**, 809 (2019).
[110] M. Simoncelli, N. Marzari, and F. Mauri, Phys. Rev. X **12**, 041011 (2022).
[111] G. Caldarelli, M. Simoncelli, N. Marzari, F. Mauri, and L. Benfatto, Phys. Rev. B **106**, 024312 (2022).
[112] E. Di Lucente, M. Simoncelli, and N. Marzari, Phys. Rev. Res. **5**, 033125 (2023).
[113] P. Giannozzi, S. Baroni, N. Bonini, M. Calandra, R. Car, C. Cavazzoni, D. Ceresoli, G. L. Chiarotti, M. Cococcioni, I. Dabo *et al.*, J. Phys. Condens. Matter **21**, 395502 (2009).
[114] P. Giannozzi *et al.*, J. Phys. Condens. Matter **29**, 465901 (2017).
[115] R. Cuscó, L. Artús, J. H. Edgar, S. Liu, G. Cassabois, and B. Gil, Phys. Rev. B **97**, 155435 (2018).
[116] M. Van Setten, M. Giantomassi, E. Bousquet, M. J. Verstraete, D. R. Hamann, X. Gonze, and G.-M. Rignanese, Comput. Phys. Commun. **226**, 39 (2018).
[117] O. O. Kurakevych and V. L. Solozhenko, Acta Crystallogr. Sect. C **63**, i80 (2007).
[118] S. Gražulis, D. Chateigner, R. T. Downs, A. F. T. Yokochi, M. Quirós, L. Lutterotti, E. Manakova, J. Butkus, P. Moeck, and A. Le Bail, J. Appl. Crystallogr. **42**, 726 (2009).
[119] S. Baroni, S. de Gironcoli, A. Dal Corso, and P. Giannozzi, Rev. Mod. Phys. **73**, 515 (2001).
[120] K. Balasubramanian, F. Hayot, and W. F. Saam, Phys. Rev. A **36**, 2248 (1987).
[121] O. Dardis and J. McCloskey, Phys. Rev. E **57**, 4834 (1998).
[122] D. Bresch and B. Desjardins, Commun. Math. Phys. **238**, 211 (2003).
[123] X. Cai and Q. Jiu, J. Math. Anal. Appl. **343**, 799 (2008).

[124] Z. Zhang, X. Wu, and M. Lu, J. Math. Anal. Appl. **377**, 414 (2011).
[125] H. Brenner, Physica (Amsterdam) **349A**, 60 (2005).
[126] J. Schwarz, K. Axelsson, D. Anheuer, M. Richter, J. Adam, M. Heinrich, and R. Schwarze, SoftwareX **22**, 101378 (2023).
[127] N. Dongari, A. Sharma IITK, and F. Durst, Microfluid. Nanofluid. **6**, 679 (2009).
[128] C. Cattaneo, Comptes Rendus **247**, 431 (1958).
[129] M. Simoncelli, Ph. D. thesis, EPFL, 2021, 10.5075/epfl-thesis-8158.
[130] We note that the VHE have a mathematical form analogous to the damped and diffusion-extended Navier-Stokes equations, used to describe rarefied fluids flowing in porous media in isothermal and laminar conditions, with VHE's temperature mapping to fluid's pressure and VHE's drift velocity mapping to fluid velocity. To see this, we highlight how the linear damping term $-\gamma^{ij}u^j(\boldsymbol{r},t)$ appearing in the second VHE (2) is analogous to the dissipative term appearing in the linearized "damped" Navier-Stokes equations [120–124] for fluids flowing through a porous medium. Then, the diffusive term appearing in the first VHE (1) $-\kappa_D^{ij}\{[\partial^2 T(\boldsymbol{r},t)]/[\partial r^i \partial r^j]\}$ is analogous to the self-diffusion term appearing for pressure in the extended Navier-Stokes equations [85,125,126] used to describe the flow of an isothermal, compressible, and rarefied gas [127].
[131] The DPLE encompasses Cattaneo's second-sound equation [128] as a special case, as discussed in SM II and [42].
[132] We investigate monoisotopic $h^{11}BN$ because Refs. [6,129] suggest that heat hydrodynamics in $h^{11}BN$ is stronger than in hexagonal boron nitride with natural isotopic-mass disorder (19.9% ^{10}B and 80.1% ^{11}B).
[133] A. Aharon-Steinberg, T. Völkl, A. Kaplan, A. K. Pariari, I. Roy, T. Holder, Y. Wolf, A. Y. Meltzer, Y. Myasoedov, M. E. Huber, B. Yan, G. Falkovich, L. S. Levitov, M. Hücker, and E. Zeldov, Nature (London) **607**, 74 (2022).
[134] F. Menges, H. Riel, A. Stemmer, and B. Gotsmann, Rev. Sci. Instrum. **87**, 074902 (2016).
[135] Z. Cheng, X. Ji, and D. G. Cahill, J. Power Sources **518**, 230762 (2022).
[136] D. G. Cahill, P. V. Braun, G. Chen, D. R. Clarke, S. Fan, K. E. Goodson, P. Keblinski, W. P. King, G. D. Mahan, A. Majumdar, H. J. Maris, S. R. Phillpot, E. Pop, and L. Shi, Appl. Phys. Rev. **1**, 011305 (2014).
[137] A. Ziabari, P. Torres, B. Vermeersch, Y. Xuan, X. Cartoixà, A. Torelló, J.-H. Bahk, Y. R. Koh, M. Parsa, P. D. Ye, F. X. Alvarez, and A. Shakouri, Nat. Commun. **9**, 255 (2018).
[138] A. Reihani, Y. Luan, S. Yan, J. W. Lim, E. Meyhofer, and P. Reddy, ACS Nano **16**, 939 (2022).
[139] V. Goblot, K. Wu, E. D. Lucente, Y. Zhu, E. Losero, Q. Jobert, C. Jaramillo Concha, N. Quack, N. Marzari, M. Simoncelli, and C. Galland, Phys. Rev. Lett. **136**, 126304 (2026).
[140] L. Bocquet and J.-L. Barrat, Soft Matter **3**, 685 (2007).
[141] We recall that the curl of a gradient is zero, so Fourier's heat flux $Q^{\delta,i} = -\kappa_D^{ij}\nabla^j T$ is irrotational.
[142] C. Zhang and Z. Guo, Int. J. Heat Mass Transfer **181**, 121847 (2021).
[143] In this time-dependent simulation we choose an equilibrium temperature of 80 K to match the temperature at which transient hydrodynamic heat propagation has been observed in recent experiments [11,12].
[144] $\dot{q}(\boldsymbol{r},t)=\mathcal{H}\cdot\theta(t_{\rm heat}-t)\exp\{-[(x+x_c)^2/(2\sigma_x^2)]-[y^2/(2\sigma_y^2)]\}$. To ensure that the perturbation created causes variations within 10% of the equilibrium temperature, we used the following parameters: $\mathcal{H}=0.013\,[\mathrm{W}/(\mu\mathrm{m}^3)]$, $t_{\rm heat}=0.4ns$, $x_c=5$ μm, $\sigma_x=2$ μm, $\sigma_y=2.8$ μm.
[145] $\dot{q}(\boldsymbol{r},t)=\mathcal{H}\cdot[\sin(2\pi f t)+1]\exp\{-[(x+x_c)^2/(2\sigma_x^2)]-[y^2/(2\sigma_y^2)]\}+\mathcal{H}\cdot[\sin(2\pi f t+\pi)+1]\exp\{-[(x-x_c)^2/(2\sigma_x^2)]-[y^2/(2\sigma_y^2)]\}$.
[146] The simulations in Fig. 3 were performed accounting for grain-boundary scattering as in Ref. [37], and considering a grain size of 20 μm. This value was estimated considering the largest grains in Fig. S3 of Ref. [11], Fig. S1 of Ref. [12], Fig. S11 of Ref. [13], and Fig. 1(e) of Ref. [6], which are all in broad agreement with 20 μm.
[147] Experiments [13] for isotopically purified graphite are available only at temperatures higher than 100 K, preventing us from comparing VHE and DPLE in the low-temperature limit, where Figs. 4(a) and 4(b) show that viscous effects are largest.
[148] Refs. [11,13] quantified the hydrodynamic strength as the dip depth of the transient thermal grating signal, see, e.g., Fig. 1(a) in Ref. [13].
[149] G. F. Nataf, S. Volz, J. Ordonez-Miranda, J. Íñiguez González, R. Rurali, and B. Dkhil, Nat. Rev. Mater. **9**, 530 (2024).
[150] F. Torres, A. C. Basaran, and I. K. Schuller, Adv. Mater. **35**, 2205098 (2023).
[151] J. Dragašević, B. Rajkov, and M. Simoncelli, Materials Cloud Archive, 10.24435/materialscloud:qh-15 (2026).

End Matter

Appendix: Temperature inversion and backflow from LBTE—In this Section we solve the space-dependent LBTE with full scattering operator in the tunnel-chamber geometry of Fig. 1. We rely on the deviational Monte Carlo solver provided in the BTE-BARNA software package [53], computing the scattering operator in the three-dimensional Brillouin zone of graphite, and simulating a device effectively infinite in the off-plane direction (i.e., with transport taking place in-plane and with temperature and heat flux depending only on the in-plane coordinates x, y), as in Fig. 1. Computational details are reported in Supplemental Material.

Figure 5 shows that the viscous temperature inversion and vorticity predicted by the VHE around $\bar{T}=70$ K (Fig. 1(b)) is predicted also by the space-dependent solution of the LBTE with full collision matrix. The

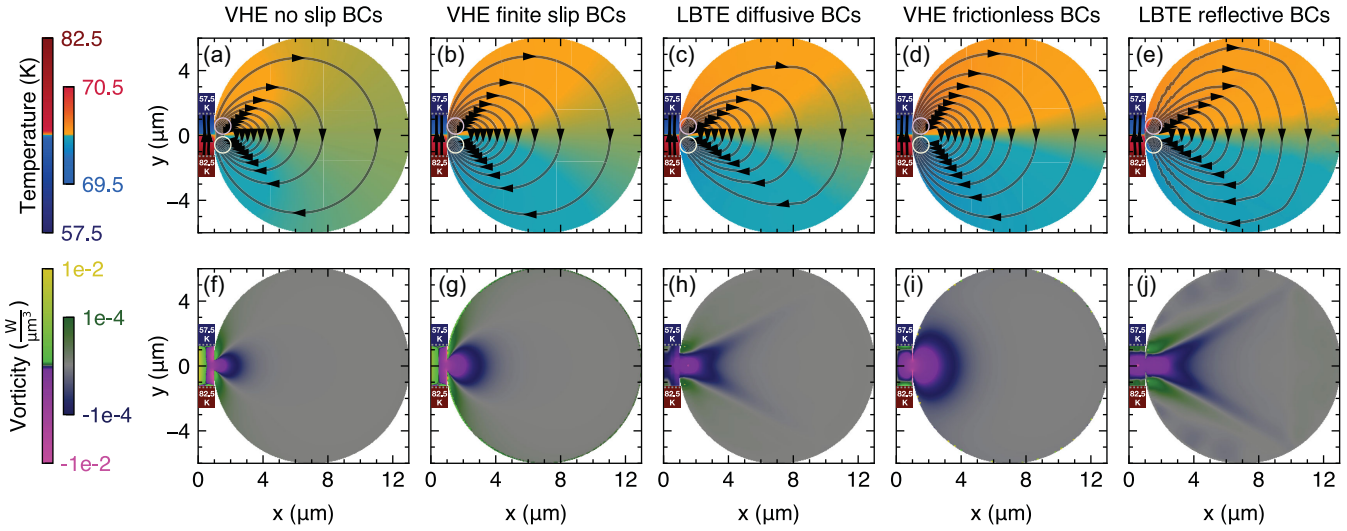


FIG. 5. Viscous heat backflow and temperature inversion from VHE and LBTE, and dependence on BCs. Top row: in-plane $(x-y)$ heat flow (streamlines) and temperature (colormap); bottom row: vorticity. All panels show a tunnel-chamber device made of natural graphite having a temperature difference applied to the tunnel (i.e., tunnel's boundaries at $y = \mp 1.25$ μm are thermalized at 70 ± 12.5 K). The nonthermalized boundaries are always adiabatic—i.e., $\boldsymbol{Q}^{\mathrm{TOT}} \cdot \hat{\boldsymbol{n}} = 0$, where $\hat{\boldsymbol{n}}$ is the unit vector orthogonal to the boundary—and each column shows the solution of VHE or LBTE for BCs exerting different friction on the total heat-flux component tangential to the boundary: (a) idealized no-slip BCs $\boldsymbol{u} = 0$ within VHE; (b) more realistic, 0.4 μm finite-slip-length BCs within mesoscopic VHE, corresponding to microscopic diffusive phonon-boundary scattering [53] within LBTE (c, see text); d and e are idealized, frictionless boundaries, corresponding to zero-shear-stress BCs within VHE (d) and reflective phonon-boundary scattering [54] within LBTE (e). The thistle and beige circle of diameter 1 μm in the top and bottom parts of the chamber (centered at $x = 1.02$ μm, $y = \pm 0.58$ μm), respectively, are temperature probes that contain the local maxima (thistle) and minima (beige) of the temperature profile, highlighting that the emergence of viscous backflow implies a temperature gradient in the chamber inverted compared to the tunnel, with inversion being stronger as the boundaries' friction is reduced from left to right. We highlight how VHE and LBTE yield a heat flux with closed streamlines, a sufficient condition to have nonzero vorticity, as confirmed by the bottom row.

LBTE is solved starting from a uniform temperature $T(x, y) = \bar{T}$ in the device interior, applying a temperature difference of 25 K at the boundaries of the tunnel (i.e., 82.5 K at the tunnel's boundary at $y = -1.25$ μm, and 57.5 K at $y = 1.25$ μm), while all other boundaries are treated as adiabatic (i.e., heat cannot cross the boundary) and with a specified phonon-momentum reflectivity (more on this later). As time evolves, heat flows into the tunnel and enters into the chamber, and the temperature profile reaches the steady state. As shown in Fig. SF 7 in Supplemental Material, the system is effectively in steady state for $t \gtrsim 1.5$ ns, and Fig. 5 reports the temperature and heat flux averaged over the steady-state window, i.e., $t \in [2, 5.5]$ ns.

The aforementioned adiabatic condition imposed on boundaries not in contact with thermal reservoirs is not sufficient to fully determine the problem; an additional assumption about phonon-boundary scattering is required. We therefore simulate the two limiting cases: diffusive and reflective boundaries [27,54]. The diffusive case (Figs. 5(c) and 5(h)) does not conserve phonon momentum, as the final phonon state is randomly selected from a Lambert cosine-law distribution [27,55]. The reflective case [Figs. 5(e) and 5(j)], in contrast, conserves the tangential component of momentum while reflecting the normal component [56]. Comparing panels c and e, it is evident that reflective BCs yield a stronger temperature inversion than diffusive BCs (see Fig. SF 7 in Supplemental Material), which is also accompanied by the reflective case (j) having vorticity larger than the diffusive case (h).

At the mesoscopic VHE level, the adiabatic BC can be imposed by requiring that the temperature-gradient and drift-velocity heat-flux components orthogonal to the boundary vanish. The first condition on the temperature gradient ($\nabla T \cdot \hat{\boldsymbol{n}} = 0$, where $\hat{\boldsymbol{n}}$ is the unit vector orthogonal to the boundary) is ubiquitously used when solving Fourier's equation, while the second condition on the drift velocity requires additional discussion. In our previous work [37] we considered the "no-slip" condition for the drift velocity, i.e., $\boldsymbol{u} = \boldsymbol{0}$ at the boundary, corresponding to phonon-boundary scattering completely dissipating the crystal momentum. More generally, one can satisfy the adiabatic BCs by imposing $\boldsymbol{u} \cdot \hat{\boldsymbol{n}} = 0$ (no hydrodynamic heat flux across the boundary, corresponding to the impermeability condition in fluid dynamics) while allowing the drift-velocity component tangential to the boundary to be nonzero, which microscopically corresponds to phonon-boundary scattering that does not fully dissipate crystal momentum.

A convenient approach to simulate partially slipping boundaries with a finite slip length b is to introduce a

lubrication layer [140] between the outer edge of the device and its interior, as in Fig. SF 5. The width of the lubrication layer w_{ll} is much smaller than the shortest lengthscale of the device. Partial slipping is then simulated by: (i) reducing shear and rotational components of the viscosity ($\eta_{\mathrm{shr}} = (\eta^{ijij} + \eta^{ijji})/2$, $\eta_{\mathrm{rot}} = (\eta^{ijij} - \eta^{ijji})/2$; see Supplemental Material VII for details) within the lubrication layer by the following slip length-dependent factor [140]

$$\frac{\eta_{\mathrm{shr}}}{\eta_{\mathrm{shr,ll}}} = \frac{\eta_{\mathrm{rot}}}{\eta_{\mathrm{rot,ll}}} = \frac{b}{w_{\mathrm{ll}}} + 1 \tag{A1}$$

and (ii) applying no-slip BCs on the side of the layer facing the device exterior. In practice, in this Letter for the tunnel-chamber geometry we choose a lubrication layer width of $w_{\mathrm{ll}} = 0.02$ μm, and by changing $\eta_{\mathrm{shr,ll}}$ ($\eta_{\mathrm{rot,ll}}$) from η_{shr} (η_{rot}) to 0 we progressively transition from no-slip ($b = 0$, a and f) to finite-slip ($b = 0.4$ μm, b and g) to frictionless ($b = \infty$, e and j) BCs. No-slip BCs are realistic when the mean free path (MFP) of the microscopic excitations is orders of magnitude smaller than the device size; finite-slip BCs instead must be considered in rarefied fluids that do not satisfy this criterion (e.g., when the MFP is comparable to the device size) [57].

Since the drift velocity originates from the average phonon momentum, the frictionless BCs can be regarded as the mesoscopic counterpart of the microscopic reflective BCs. Comparing panels d and e, and Fig. SF 7a in the SM, we see that the temperature emerging from the frictionless VHE and reflective LBTE are in quantitative agreement, confirming this. The slip length 0.4 μm used in (b) was obtained by comparing the difference in temperature inversion between the reflective (e) and diffusive LBTE (c), and progressively increasing η_{ll} in Eq. (A1) from zero to a value yielding the same difference between the frictionless VHE (d) and finite-slip VHE (b).

We note that the vorticity predicted by the finite-slip VHE (g) and the diffusive LBTE (h) is in closer agreement than that between the frictionless VHE and reflective LBTE (i), (j). In particular, the differences between frictionless VHE and reflective LBTE vorticities are more pronounced near the chamber opening, where the geometry and magnitude of the heat flux are most nonuniform. These vorticity discrepancies might originate from discarding spatial gradients of the out-of-equilibrium phonon distribution when coarse-graining the LBTE into the VHE [37]; they have a weak ($\lesssim$10%) effect on the agreement between the VHE and LBTE predictions for the experimentally measurable temperature inversion (Fig. SF 7 in Supplemental Material). Even though spatial gradients of the out-of-equilibrium phonon distribution are discarded in the VHE derivation, the VHE still encode a weakly nonlocal constitutive relation between heat flux and temperature gradient. Specifically, we show in Supplemental Material III that the VHE encompass the GKE as a special limit, and Ref. [58] shows that the GKE yield a weakly nonlocal constitutive relation in the presence of a nonzero nonlocal length $l_\eta = \sqrt{\eta/\gamma}$. Reference [33] discussed how the weakly nonlocal GKE can capture nonlocal effects emerging in nanoscale devices. It is also worth mentioning that nonlocal effects are not necessarily related to a nonzero viscosity; they can also emerge in the ballistic regime from the term $\nabla n_\nu^\delta(\boldsymbol{r}, t)$ that is not retained in the VHE derivation [59]. For the materials, geometries, and temperatures considered here, we show that accounting for the weakly nonlocal effects emerging from viscosity is sufficient to obtain good agreement with the full LBTE.

It is worth mentioning that the derivation of the VHE focuses on the close-to-equilibrium linear regime and therefore neglects nonlinear advection terms. These have so far been discussed only (i) within the Callaway-approximated LBTE for temperature waves in two-dimensional materials [60], and (ii) in a recent study that benchmarked analytical predictions against a numerical Monte Carlo solution of the LBTE under the relaxation-time approximation [61]. Accounting for these nonlinear effects analytically and numerically while using the full LBTE collision matrix remains an open problem beyond the scope of this Letter.

We conclude by noting that our results share fundamental common underpinnings with other quasiparticle's fluidlike transport phenomena in solids—involving, e.g., electrons [62,133] coupled with phonons [63–70], magnons [71], and skyrmions [72]—thus may inspire analogous applications in these areas.